JOURNAL OF GEOPHYSICAL RESEARCH, VOL. 112, A10224, doi:10.1029/2007JA012522, 2007

Sources, transport, and distributions of plasma sheet ions and electrons and dependences on interplanetary parameters under northward interplanetary magnetic field

Chih-Ping Wang,[1] Larry R. Lyons,[1] Tsugunobu Nagai,[2] James M. Weygand,[3] and Richard W. McEntire[4]

Received 3 May 2007; revised 13 June 2007; accepted 3 August 2007; published 30 October 2007.

[1] We have investigated the Geotail data statistically to understand the particle sources, transport, and spatial distributions of the plasma sheet ions and electrons of different energies during northward interplanetary magnetic field (IMF), and their dependences on the solar wind density (N_{sw}), the solar wind speed (V_{sw}), and the magnitude of the northward IMF B_z ($|B_{z,IMF}|$). We find that the plasma sheet becomes colder and denser, indicating a larger increase in the cold than in the hot population, with increasing N_{sw} or $|B_{z,IMF}|$ or with decreasing V_{sw}. The cold population dominates the region near the flanks while the hot population dominates the near-midnight region, which is consistent with the plasma sheet plasma being a mixture of cold particles coming from the flanks and hot particles from the distant-tail. The phase space densities show that the flank source strongly depends on $|B_{z,IMF}|$, while the tail source strongly depends on V_{sw}. Cold particles from the dawn flank to midnight increase significantly with decreasing V_{sw}, but no significant changes are seen near the dusk flank, suggesting a dependence of the solar wind entry through the dawn flank on V_{sw}. The comparisons between the distributions of the phase space density and the electric and magnetic drift paths estimated from the observations indicate that the thermal and high-energy particles are mainly transported by electric and magnetic drift, while other transport mechanisms, such as diffusion, may play a role in transporting the low energy particles from the flank sources to midnight.

Citation: Wang, C.-P., L. R. Lyons, T. Nagai, J. M. Weygand, and R. W. McEntire (2007), Sources, transport, and distributions of plasma sheet ions and electrons and dependences on interplanetary parameters under northward interplanetary magnetic field, *J. Geophys. Res.*, *112*, A10224, doi:10.1029/2007JA012522.

1. Introduction

[2] The plasma sheet is colder and denser during northward interplanetary magnetic field (N IMF) than southward IMF (S IMF) [e.g., *Terasawa et al.*, 1997; *Wing and Newell*, 2002, 2005]. Despite geomagnetic activity being low during N IMF periods, the more abundant cold plasma that builds up during N IMF can provide more source particles for the inner magnetosphere than under S IMF and lead to a stronger ring current and geomagnetic disturbances after a sudden southward IMF [*Thomsen et al.*, 2003; *Lavraud et al.*, 2006]. Thus the N IMF plasma sheet can play a crucial pre-conditioning role in the development of storms and substorms, and related geomagnetic activity during S IMF. Therefore it is important to understand the distributions of N IMF plasma sheet plasma, the particle sources and transport that result in these distributions, and how the distributions depend on different interplanetary parameters.

[3] The spatial structure of the plasma sheet plasma is determined by the locations and strengths of the different particle sources, and the transport paths of particles of different energies. The major particle sources for the plasma sheet are believed to be the mantle particles entering through the distant tail and the magnetosheath particles entering through the flank magnetopause. The particles from the mantle, after energization through current sheet crossing [*Lyons and Speiser*, 1982], have higher temperatures than the particles from the flank magnetosheath. The major large-scale transport of the plasma sheet plasma consists of energy-independent electric drift and energy-dependent magnetic drift [*Spence and Kivelson*, 1993; *Wang et al.*, 2006]. Other likely transport processes during N IMF include diffusion [*Terasawa et al.*, 1997] and fast flows [e.g., *Garner et al.*, 2003; *Kaufmann et al.*, 2004], however, their contributions are not well understood.

[4] Ion entry from the flanks appears to be more efficient during northward IMF than southward IMF [e.g., *Fujimoto*

[1]Department of Atmospheric and Oceanic Sciences, University of California, Los Angeles, California, USA.
[2]Department of Earth and Planetary Sciences, Tokyo Institute of Technology, Tokyo, Japan.
[3]Institute of Geophysics and Planetary Physics, University of California, Los Angeles, California, USA.
[4]Applied Physics Laboratory, Johns Hopkins University, Laurel, Maryland, USA.

0148-0227/07/2007JA012522$09.00

Table 1. The Ranges (Values Inside the Brackets), Averages, and Standard Deviations of the Solar Wind Density (N_{sw}), Solar Wind Speed (V_{sw}), and the Magnitude of the Northward IMF B_z ($|B_{z,IMF}|$) for the 8 Interplanetary Conditions

Condition	(1) N_{low} V_{low} B_{low}	(2) N_{high} V_{low} B_{low}	(3) N_{low} V_{low} B_{high}	(4) N_{high} V_{low} B_{high}	(5) N_{low} V_{high} B_{low}	(6) N_{high} V_{high} B_{low}	(7) N_{low} V_{high} B_{high}	(8) N_{high} V_{high} B_{high}
N_{sw} cm^{-3}	[0, 6.5]	[6.5, 15]	[0, 6.5]	[6.5, 15]	[0, 6.5]	[6.5, 15]	[0, 6.5]	[6.5, 15]
	4.8 ± 1.1	9.7 ± 2.3	4.8 ± 1.2	9.6 ± 2.1	3.8 ± 1.3	8.8 ± 2.0	3.7 ± 1.5	8.9 ± 2.1
V_{sw} 10^2 km/s	[0, 4]	[0, 4]	[0, 4]	[0, 4]	[4, 10]	[4, 10]	[4, 10]	[4, 10]
	3.6 ± 0.3	3.5 ± 0.3	3.6 ± 0.2	3.6 ± 0.3	5.1 ± 0.9	4.4 ± 0.4	5.1 ± 0.9	4.5 ± 0.5
$\|B_{z,IMF}\|$ nT	[0, 1.3]	[0, 1.3]	[1.3, 8]	[1.3, 8]	[0, 1.3]	[0, 1.3]	[1.3, 8]	[1.3, 8]
	0.6 ± 0.3	0.6 ± 0.4	2.5 ± 1.0	2.8 ± 1.5	0.6 ± 0.4	0.6 ± 0.4	2.5 ± 1.1	2.9 ± 1.4

et al., 1998]. Previous studies [e.g., *Borovsky et al.*, 1998; *Tsyganenko and Mukai*, 2003] showed that the plasma sheet ion density is highly correlated with the solar wind density and that the plasma sheet ion temperature is highly correlated with the solar wind velocity. *Terasawa et al.* [1997] showed that the plasma sheet becomes denser and colder with higher northward IMF B_z. The spatial structure of the plasma sheet is shown to be very different under different IMF B_z conditions [*Wing and Newell*, 2002; *Wang et al.*, 2006]. These previous studies only focused on ions, thus our understanding of the electron plasma sheet is still limited. Furthermore, these studies mainly focused on the changes in plasma moments, which can be affected by both the changes in particle sources and magnetic field configurations. Therefore investigations of phase space density is necessary to understand if the dependences of the particle sources to the plasma sheet on the interplanetary parameters can account for the observed solar wind-plasma sheet correlations indicated in these studies.

[5] In this paper, we first investigate statistically 11 years of Geotail observations of the distributions of ion and electron density, temperature, pressure, and magnetic fields, and how theses distributions respond separately to a change in solar wind density, solar wind speed, or the magnitude of the northward IMF B_z. We then investigate the phase space density versus particle energy to exclude changes in the plasma moments due to changes in the magnetic field configuration in order to understand how the major particle sources change with the interplanetary conditions and the implications of these changes on the solar wind entry. We compare the distributions of phase space density with electric and magnetic drifts evaluated from the observations to determine if the observed distributions at different energies can be accounted for by the expected electric and magnetic drift transport of particles from the flank and tail sources. We furthermore discuss if the conditions in the plasma sheet are suitable for diffusion to transport low energy particles toward midnight from the flanks, and how different distributions of N IMF plasma sheet plasma, as source particles for the ring current, can result in a very different storm-time ring current.

2. Instrumentation and Data

[6] In this study we use Geotail data in aberrated GSM coordinates (with the aberration angle determined by one hour averaged solar wind velocity) from 1 January 1995 to 31 December 2005 and in the area $|Y| \leq 22.5\ R_E$ and $0 \geq X \geq -30\ R_E$ (the smallest radial distance covered by Geotail is $\sim 8\ R_E$). Plasma data from two instruments aboard Geotail are used: the ion and electron data from the Low Energy Particle (LEP) instrument [*Mukai et al.*, 1994] that covers the ion energy range from 21 eV/q to 44 keV/q and the electron energy range from 43 eV to 41 keV, and the proton data from the Energetic Particles and Ion Composition (EPIC) instrument [*Williams et al.*, 1994] that covers the energy range from 46 keV to 3005 keV. Magnetic field data is from the magnetic field (MGF) experiment [*Kokubun et al.*, 1994]. The ion density, temperature, and pressure are a summation of the LEP and EPIC moments. The ion and electron count data in four directions (sunward, duskward, anti-sunward, dawnward) are used in the study of phase space density and are used to obtain the electron moments. 1 min averages of the plasma and magnetic field data are used.

[7] We used the solar wind and IMF data mainly from Wind. The arrival time of the IMF at the subsolar bow shock at ($X = 17$, $Y = 0$, $Z = 0\ R_E$) is determined by calculating the minimum variance direction using the minimum variance analysis technique [*Weimer et al.*, 2003]. During times when the Wind data is not available or the propagated Wind data is not reliable due to the Wind's position (when Wind is more than $\sim 50\ R_E$ off the Sun-Earth), we used the solar wind and IMF data from ACE, which is available after February 1998.

[8] The plasma sheet is centered at the equatorial plane. Central plasma sheet crossings are defined by plasma pressure (P_{ion}) being larger than magnetic pressure ($P_{mag} = B^2/(2\mu_0)$). We use $V_x > -100$ km/s to exclude magnetosheath crossings and $|V_\perp| \leq 200$ km/s to exclude large bursty bulk flow. The interplanetary parameters are averaged over 8 h prior to the Geotail observations. Eight hours is a typical timescale for good correlations between the plasma sheet and the IMF B_z direction [*Terasawa et al.*, 1997; *Øieroset et al.*, 2003]. The data for the central plasma sheet are then sorted into 8 different interplanetary conditions with each condition a combination of three interplanetary parameters (solar wind density (N_{sw}), solar wind speed (V_{sw}), and the magnitude of the northward IMF B_z ($|B_{z,IMF}|$)) in their low or high value range. The 8 conditions are listed in Table 1. By comparing the difference in the plasma sheet distributions when one of the three parameters is changed from its low to high value and with the other two parameters unchanged, we can approximately investigate the effect from changes in each individual parameter. Finally the sorted data are averaged over an area of $2.5\ R_E \times 2.5\ R_E$ in the X-Y plane. The electron temperature and pressure are computed from two-component kappa distributions that we obtained from fitting the averaged phase space density data within each X-Y bin as described in section 3.2.

3. Results and Analysis

[9] In this section we first present the distributions of plasma moments and magnetic field, and their changes with

different interplanetary conditions. We show the plasma sheet population as a mixture of cold and hot populations presumably from different source locations. We then present the phase space density versus particle energy and offer explanations for the changes in the observed moments from likely changes in the particle sources along the flanks and at the tail and their implications for the solar wind entry.

3.1. Number Density, Temperature, Pressure, and Magnetic Fields

[10] Figure 1 shows the number of data measurements, plasma moments, and magnetic fields, for the 8 interplanetary conditions listed in Table 1. There are more than 100 data measurements inside each $2.5 \times 2.5\ R_E^2$ region in most of the plasma sheet for each condition except for condition (6).

3.1.1. Number Density and Temperature

[11] The overall plasma sheet number density (N_{ps}) is higher when N_{sw} or $|B_{z,IMF}|$ is higher. However, the overall N_{ps} is lower when V_{sw} is higher, which is a result of V_{sw} and N_{sw} being anti-correlated, as indicated in the average N_{sw} for the low and high V_{sw} in Table 1. The dependence of N_{ps} on N_{sw} indicates that the solar wind is the major particle source for the plasma sheet during N IMF. The overall normalized density N_{ps}/N_{sw} is higher when N_{sw} or V_{sw} is lower and is higher when $|B_{z,IMF}|$ is higher. The density is higher near the flanks and lower near midnight under all conditions. The density near the dawn flank is higher (lower) than those near the dusk flank when V_{sw} is lower (higher).

[12] The overall plasma sheet temperature (T_{ps}) for both ions and electrons is higher when V_{sw} is higher, and is lower when N_{sw} or $|B_{z,IMF}|$ is higher. The dependence on N_{sw} could be partly due to V_{sw} being slightly lower when N_{sw} is higher. T_{ps} is higher near midnight than near the flanks, and the ion T_{ps} (electron T_{ps}) in the pre-midnight sector is higher (lower) than that in the post-midnight sector in the near-Earth plasma sheet. The dawn-dusk asymmetry is stronger when V_{sw} is higher. Large ion-to-electron temperature ratios (>20) are seen near the dusk flank, while small ratios (<5) are seen in the post-midnight sector of the near-Earth plasma sheet. These dawn-dusk asymmetries and the locations of the maximum and minimum temperature ratios, as discusses in Section 4.2 are consistent with the expectation of ion's (electron's) duskward (dawnward) magnetic drift.

[13] That the region of higher N_{ps} (or N_{ps}/N_{sw}) coincides with lower T_{ps}, and plasma is colder and denser toward the flanks is consistent with the picture that the particles coming from the flank, which are colder than the particles from the tail, become more dominant closer to the flanks. The response of the cold and dense plasma near the flanks to the changes in the interplanetary parameters reflects the changes in the flank source.

3.1.2. Pressure

[14] The overall plasma sheet pressure (P_{ps}) is higher for higher Nsw, V_{sw}, or $|B_{z,IMF}|$. The correlations between P_{ps} and N_{sw} or V_{sw} can be explained by the compression effect of solar wind dynamic pressure (P_{dyn}). The P_{ps} is relatively uniform across the tail in the mid-tail region. In the near-Earth region, the ion pressure is slightly higher in the pre-midnight sector under most of the conditions, while the total plasma pressure (ion plus electron) is more dawn-dusk symmetric than the ion pressure.

3.1.3. Magnetic Fields

[15] The plasma sheet B_z is higher when N_{sw}, V_{sw}, or $|B_{z,IMF}|$ is higher. The effect of N_{sw} and V_{sw} on B_z is likely to be the result of magnetosphere compression by P_{dyn}. The B_z is higher near the flanks than near midnight and the B_z near the dawn flank is always higher than that near the dusk flank. The B_z dawn-dusk asymmetry indicates a dawn-dusk asymmetry in the magnetic field configuration, and therefore a likely dawn-dusk asymmetry in the magnetic flux tube volume.

3.1.4. Factors Contributed to the Changes in Moments

[16] The above solar wind-plasma sheet correlations are consistent with the previous studies mentioned in the introduction. From our understanding that the majority of the plasma sheet particles during N IMF come from the solar wind, the above overall changes in the plasma moments throughout the plasma sheet should reflect changes in the particle sources and give indications on how the efficiency of the solar wind entry to the flanks and distant tail varies with interplanetary parameters. However, changes in magnetic field configuration and the associated magnetic flux tube volume (as indicated by the changes in the plasma sheet B_z) also result in changes in plasma density and temperature. Therefore it is necessary to investigate the phase space density versus different energy invariants so that the effect of magnetic field configuration changes is approximately excluded in order to understand how the interplanetary parameters affect the strength of the colder particle source along the flanks and the hotter particle source at the tail.

3.2. Mixtures of Cold and Hot Populations

[17] Count rate statistics limit the reliability of LEP instrument measuring very low energy ions (<0.1 keV), especially when the plasma temperature is high. In order to more accurately estimate the phase space density of low energy particles from the observations, we fit the observed ion and electron energy spectrum (0.1 to 100 keV for ions and 0.04 to 40 keV for electrons) averaged in each $2.5 \times 2.5\ R_E^2$ region with a two-component (one to represent cold population and one to represent hot population) kappa distribution,

$$f = N_c\left(\frac{m}{2\pi\kappa_c E_{0,c}}\right)^{3/2}\frac{\Gamma(\kappa_c+1)}{\Gamma(\kappa_c-1/2)}\left[1+\frac{E}{\kappa_c E_{0,c}}\right]^{-\kappa_c-1} + N_h\left(\frac{m}{2\pi\kappa_h E_{0,h}}\right)^{3/2}\frac{\Gamma(\kappa_h+1)}{\Gamma(\kappa_h-1/2)}\left[1+\frac{E}{\kappa_h E_{0,h}}\right]^{-\kappa_h-1},$$

where N is density, m is particle mass, κ and E_0 are parameters of the kappa distribution (subscript c is for cold population and h is for hot populations, E_0 is the energy of the peak particle flux). N, κ, and E_0 are free parameters in the fitting. (In the fitting of the ion spectrum, we used a fixed $\kappa_c = 4$. We first tried to include κ_c in our free parameters of the non-linear least squares fit, but the fitting did not converge in most of the cases. We then tried different fixed values for κ_c and found that $\kappa_c = 4$ gave the best overall fit.) The N for electrons is adjusted so the total electron density equals to the ion density.

[18] In addition to providing complete energy spectra, these fitted two-component kappa distributions allow us to

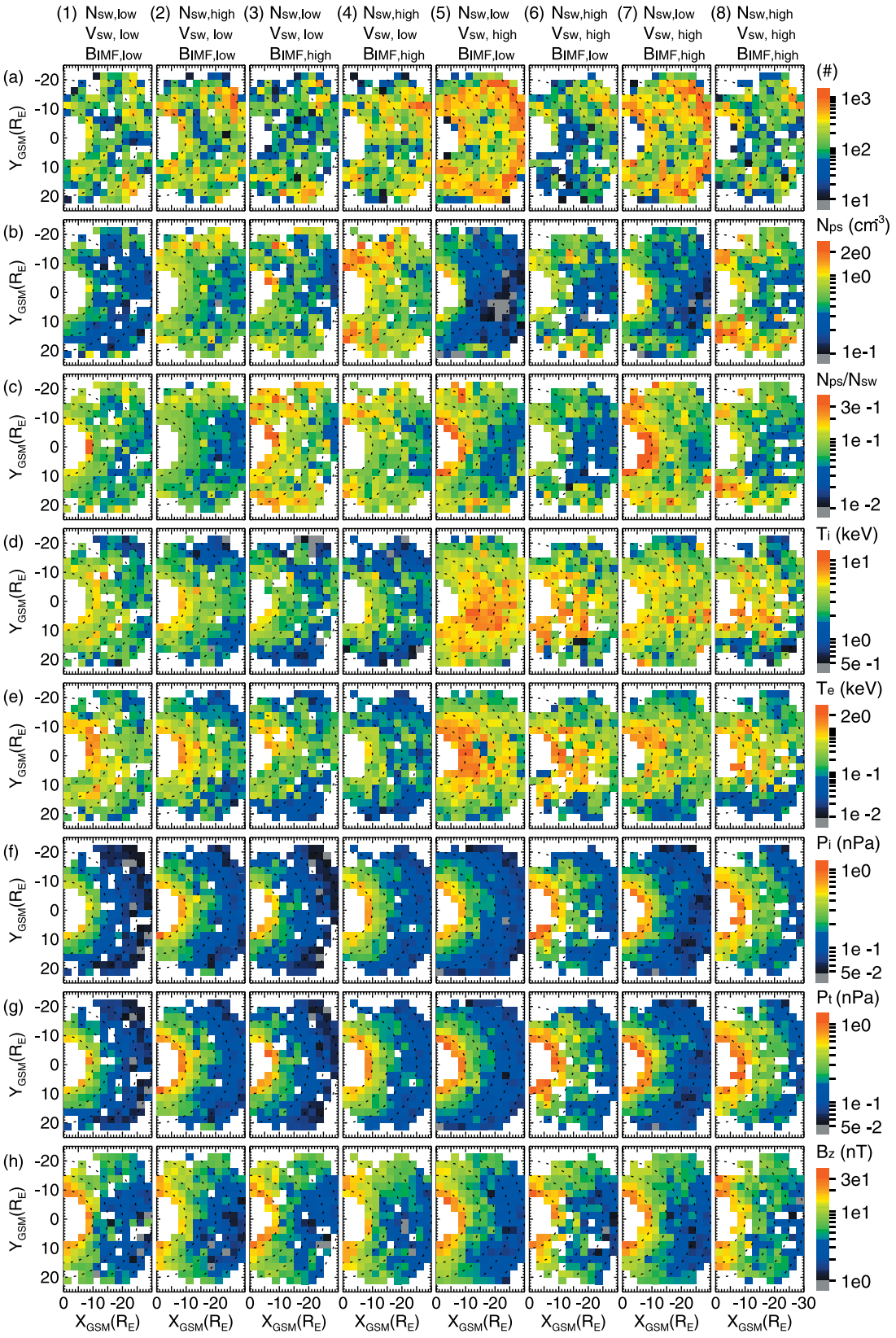

Figure 1. The equatorial distributions of (a) number of 1 min data measurements, (b) ion number density N_{ps} (cm^{-3}), (c) normalized ion number density (N_{ps}/N_{sw}), (d) ion temperature T_i (keV), (e) electron temperature T_e (keV), (f) ion pressure P_i (nPa), (g) ion plus electron pressure Pt (nPa), and (h) B_z (nT) for the 8 interplanetary conditions listed in Table 1.

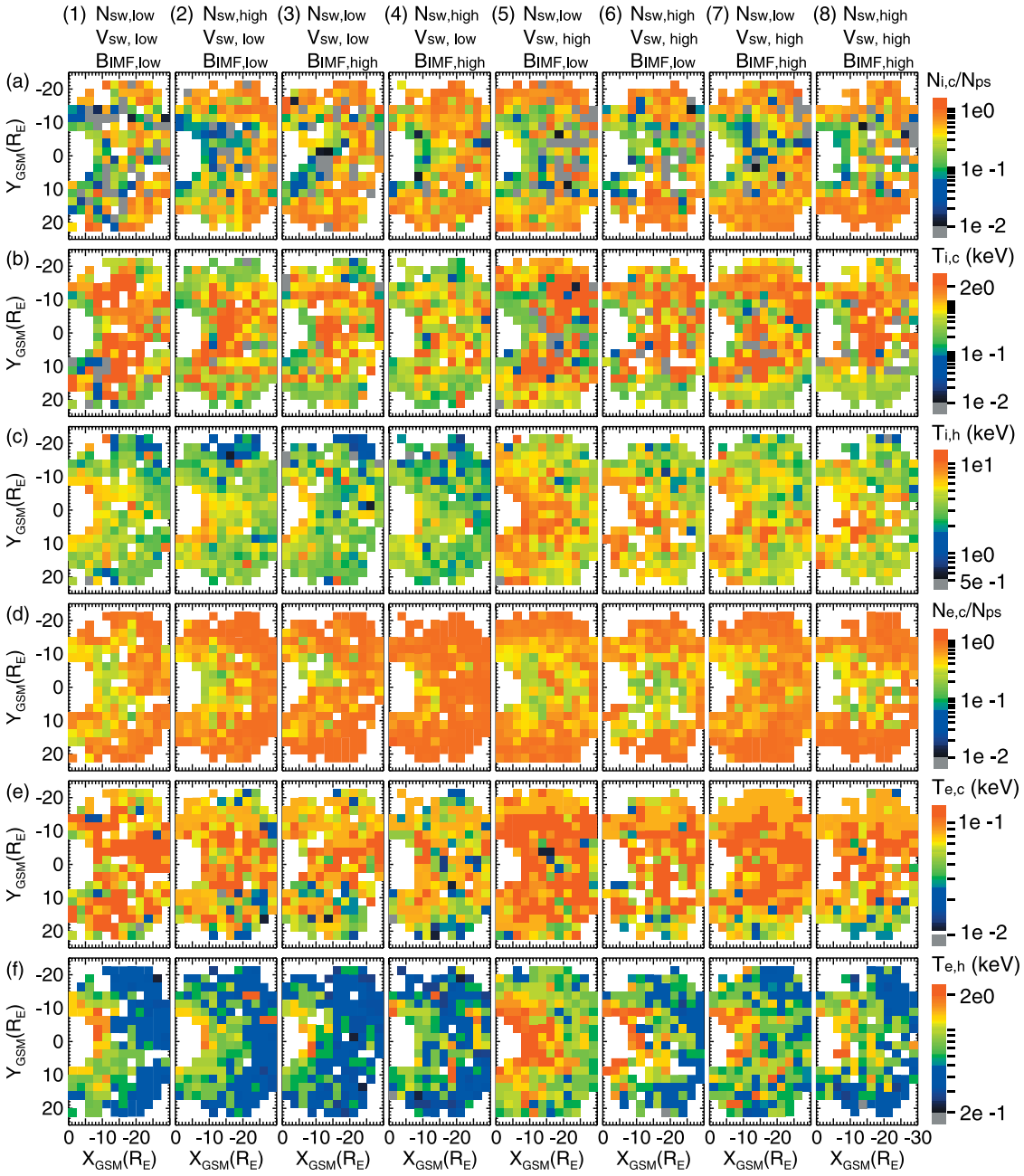

Figure 2. The equatorial distributions of (a) ratios of the density of the cold ion population $N_{i,c}$ to the total ion density N_{ps}, (b) the temperature of the cold ion population $T_{i,c}$, (c) the temperature of the hot ion population $T_{i,h}$, (d) ratios of the density of the cold electron population $N_{e,c}$ to the total electron density N_{ps}, (e) the temperature of the cold electron population $T_{e,c}$, and (f) the temperature of the hot electron population $T_{e,h}$ for the 8 interplanetary conditions.

investigate separately the distributions of the cold and hot populations and their relative contributions to the plasma sheet. Figure 2 shows the contribution of the cold population to the total density ($N_c/(N_c + N_h)$), and the temperatures of the cold and hot populations. For both ions and electrons, the contribution of the cold population significantly enhances and becomes dominant toward the flanks. In the region near midnight, the cold population has a significant contribution in the mid-tail only when V_{sw} is low. The temperature for the cold population near the dawn flank is similar to that near the dusk flank when V_{sw} is low. However, the dawn flank temperature increases much more with increasing V_{sw} than does the dusk flank temperature, resulting in higher temperature near the dawn than the dusk flank when V_{sw} is higher. This is seen in both ions and electrons. The temperature asymmetry between the dawn and dusk flank in the cold population was reported by *Wing et al.* [2006] under N IMF with all V_{sw} conditions included. In the near-Earth plasma sheet, the number density is mainly from the hot population. The temperature for the hot ion (electron) population is higher in the pre-midnight (post-midnight) sector. This shows that the temperature asymmetry shown in

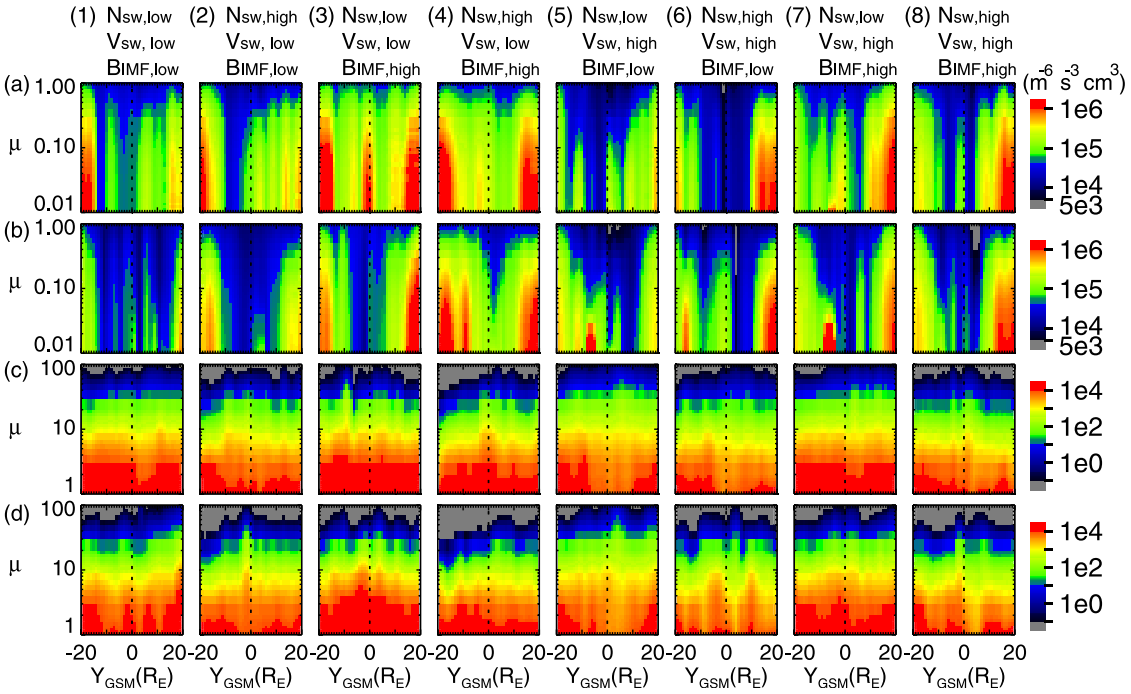

Figure 3. The *Y*-profiles of the ion phase space density normalized to the solar wind density (color bar in unit of $m^{-6}\ s^{-3}\ cm^3$) for the 8 interplanetary conditions. (a) For $\mu = 0.01$ to 1 keV/10 nT at $X = -15$ to $-30\ R_E$, (b) for $\mu = 0.01$ to 1 keV/10 nT at $X = 0$ to $-15\ R_E$, (c) for $\mu = 1$ to 100 keV/10 nT at $X = -15$ to $-30\ R_E$, (d) for $\mu = 1$ to 100 keV/10 nT at $X = 0$ to $-15\ R_E$.

Figure 1 is contributed by the high-energy particles. The distribution of the plasma sheet population therefore can be understood as a mixture of a cold and a hot population depending on the relative strengths of the flank and tail sources that changes with interplanetary conditions, as discussed in Section 3.3, and the transport paths from these two source locations, as discussed in Section 4.2.

3.3. Phase Space Density, Particle Sources, and Solar Wind Entry

[19] With the two-component kappa distributions obtained from the fitting, we computed phase space density (f) as a function of the first adiabatic invariant μ. μ is defined as E_k/B, where E_k is particle's kinetic energy. The unit for μ is chosen to be keV/10nT. Since 10 nT is approximately the field strength at $X = -15$ and $Y = 0\ R_E$, these units for μ indicate the energy that a particle would have in the plasma sheet.

[20] We normalize the phase space density to N_{sw} so that the changes of the normalized phase space density (f_N) with different interplanetary parameters can give better indication on the efficiency of the solar wind entry. The f_N versus μ for $\mu <$ and $>$ 1 keV/10nT across the tail in the near-Earth and the mid-tail plasma sheet is shown in Figure 3 for ions and Figure 4 for electrons.

[21] Important features of f_N for $\mu < 1$ keV/10 nT are:

[22] (1) For both ions and electrons, the overall f_N increases with increasing $|B_{z,IMF}|$ and the increase is stronger with decreasing particle energy. This indicates the entry of solar wind through the flanks is more efficient when the $|B_{z,IMF}|$ is higher, which results in the overall higher N_{ps} (or N_{ps}/N_{sw}) for higher $|B_{z,IMF}|$ shown in Figure 1.

[23] (2) The overall f_N in the mid-tail and in the near-Earth flank region increases slightly with increasing N_{sw}, indicating the flank source is slightly stronger when N_{sw} is higher. This dependence, however, is opposite to that of the normalized N_{sw}/N_{ps}, which is seen to decrease with increasing N_{sw} as shown in Figure 1c. This shows that changes in moments, affected also by the changes in the magnetic field configuration, may not appropriately indicate the changes in the particle sources.

[24] (3) In the mid-tail, f_N near the dawn flank and midnight is significantly higher when V_{sw} is lower, while the change of f_N near the dusk flank is not significant compared with the changes near the dawn flank. The higher f_N from the dawn flank to midnight accounts for the overall higher N_{ps} (or N_{ps}/N_{sw}) when V_{sw} is lower as shown in Figures 1b and 1c. The higher f_N near midnight in the mid-tail is likely to be due to particles from the flank, not from the distant tail, as discussed in Section 4.2. The above dependences suggest the entry of the solar wind through the dawn flank is more efficient when V_{sw} is lower, while the entry through the dusk flank does not depend on V_{sw}. However, the magnetosheath temperature decreases with decreasing V_{sw}, so there are more cold magnetosheath particles when V_{sw} is lower. This can explain the f_N changes along the dawn flank, but not that along the dusk flank. It is not clear that any mechanism for plasma entry through the flank magnetopause can explain these dependences of entry on V_{sw}. It is also not certain if the magnetosheath temperatures are dawn-dusk symmetric.

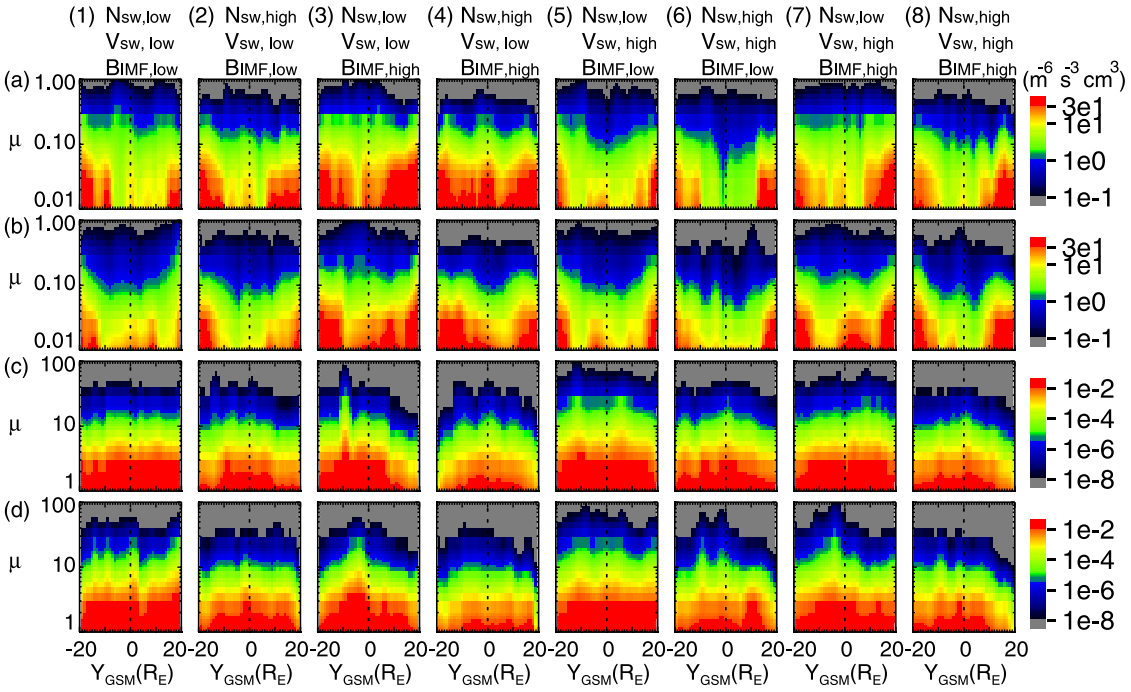

Figure 4. The *Y*-profiles of the electron phase space density normalized to the solar wind density (color bar in unit of $m^{-6}s^{-3}$ cm^3) for the 8 interplanetary conditions. (a) For $\mu = 0.01$ to 1 keV/10 nT at $X = -15$ to -30 R_E, (b) for $\mu = 0.01$ to 1 keV/10 nT at $X = 0$ to -15 R_E, (c) for $\mu = 1$ to 100 keV/10 nT at $X = -15$ to -30 R_E, (d) for $\mu = 1$ to 100 keV/10 nT at $X = 0$ to -15 R_E.

[25] (4) In general, the overall f_N in the near-Earth region is smaller than that in the mid-tail, especially in the near-midnight region, indicating the particles are pushed away from midnight as they go closer to the Earth. This is associated with transport and is further discussed in Section 4.2.

[26] Important features of f_N for $\mu > 1$ keV/10 nT are:

[27] (1) The overall f_N is higher when V_{sw} is higher for both ions and electrons in almost all the regions, which indicates the tail source is stronger for higher V_{sw}. This can be due to the entry of the mantle particles to the distant tail being more efficient, or due to an increase in the number of high-energy particles in the magnetosheath when V_{sw} is higher. This, combined with the significant decrease in the low energy f with increasing V_{sw}, accounts for the increase in T_{ps} with increasing V_{sw} shown in Figures 1d and 1e.

[28] (2) The overall f_N is slightly lower for higher N_{sw} or $|B_{z,IMF}|$. These dependences are less clear in the mid-tail near-midnight region, suggesting the tail particle source does not change with N_{sw} or $|B_{z,IMF}|$.

[29] (3) In the near-Earth region, it can be seen that the f in the pre-midnight sector is higher than that in the post-midnight sector in ions (Figure 3d), while the f for electrons is higher in the post-midnight sector (Figure 4d). These dawn-dusk asymmetries become more significant with increasing μ. This, as discussed in Section 4.2, is due to the energy and charge dependent magnetic drift. The magnetic drift also explains why large (small) ion/electron temperature ratios are seen near the dusk flank (near-Earth post midnight). The dawn-dusk asymmetry and the decrease (increase) of the low (high) energy particles with increasing V_{sw} accounts for the stronger dawn-dusk temperature asymmetries in the near-Earth plasma sheet when V_{sw} is higher as shown in Figures 1d and 1e.

[30] The above results show that the flank source strongly depends on $|B_{z,IMF}|$, while the tail source strongly depends on V_{sw}. Therefore under higher $|B_{z,IMF}|$, higher N_{sw}, and lower V_{sw}, there will be more cold particles but less hot particles from these sources, which result in a colder and denser plasma sheet. The stronger flank source under higher $|B_{z,IMF}|$ is very likely due to higher efficiency for the solar wind entry. However, even though the above results suggests the solar wind entry through the flanks (distant tail) is more efficient under higher N_{sw} (V_{sw}), it cannot be fully determined until we understand how the population in different regions of the magnetosheath changes with N_{sw} or V_{sw}.

4. Electric and Magnetic Drift Transport

[31] In this section we first estimate the plasma sheet electric field potential distribution from the ion observations. We then evaluate the electric and magnetic drift paths of different energy particles and determine if the drift transport can account for the large-scale features of the observed distributions of the phase space density at different energies.

4.1. Electric Field Potential

[32] In the slow flow approximation, which is valid within the plasma sheet except during dynamic periods such as the expansion phase of substorms, plasma drift results from electric drift $\mathbf{V}_E = (\mathbf{E} \times \mathbf{B})/B^2$ and diamagnetic drift $\mathbf{V}_{dia}$, where $\mathbf{E}$ is electric field and $\mathbf{B}$ is magnetic field. $\mathbf{V}_{dia} = (\mathbf{B} \times$

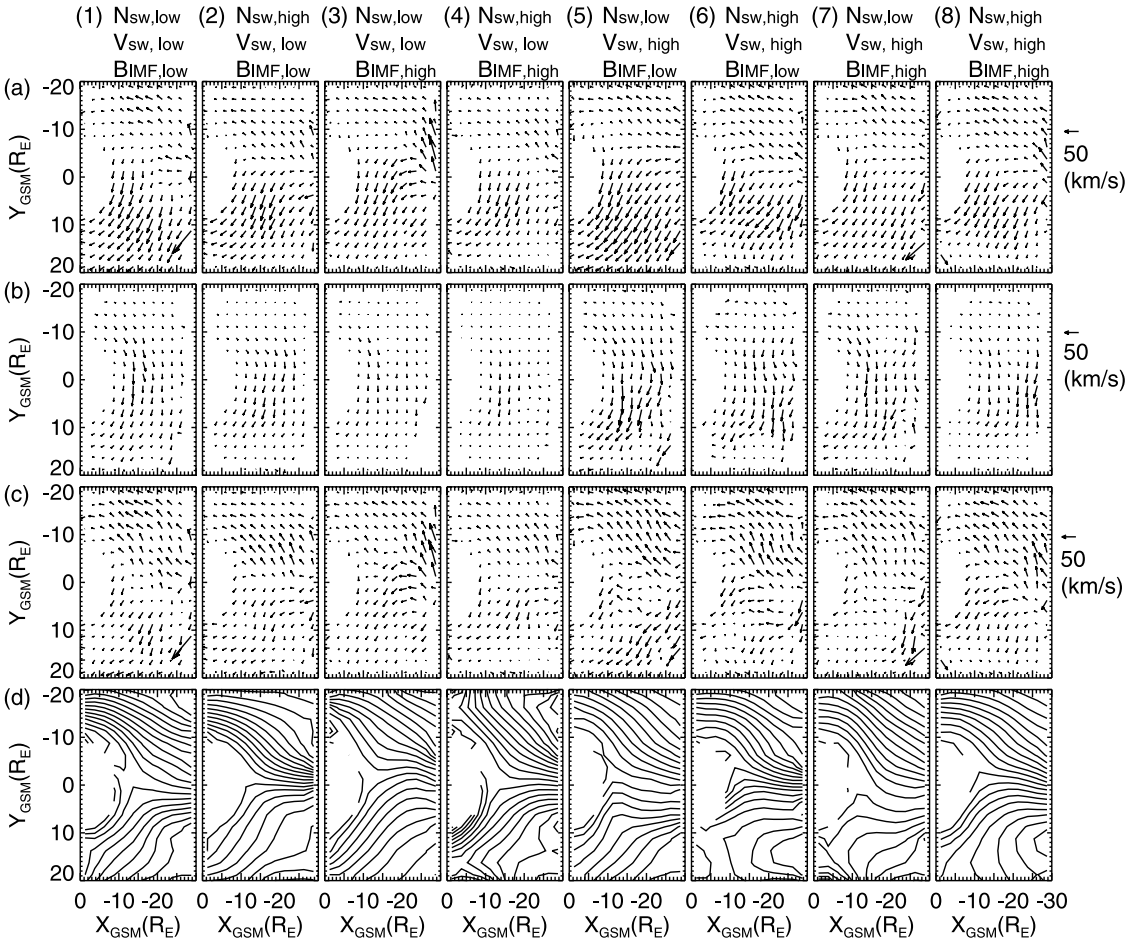

Figure 5. The equatorial distributions of (a) perpendicular flow, (b) diamagnetic drift, (c) electric drift, and (d) electric potential contours (5 kV intervals) for the 8 interplanetary conditions. The arrow at the top right corner represents a unit vector of 50 km/s.

$\nabla P_{ps})/(eN_{ps} B^2)$ for protons under the condition of isotropic pressure, which is a good approximation for the plasma sheet plasma [e.g., *Nakamura et al.*, 1991; *Kaufmann et al.*, 2005], where P_{ps} is ion pressure and N_{ps} is number density. Figure 5a shows the observed perpendicular flow $\mathbf{V}_\perp$ and Figure 5b shows $\mathbf{V}_{dia}$ in the x-y directions at the center of the current sheet ($\mathbf{B} = B_z\hat{\mathbf{z}}$) using the N_{ps} and P_{ps} distributions shown in Figures 1b and 1f assuming all ions are protons, and the B_z distributions shown in Figure 1h. N_{ps}, P_{ps} and B_z have been smoothed before computing $\mathbf{V}_{dia}$. $\mathbf{V}_{dia}$ is mainly directed westward because ∇P_{ps} is mainly in the radial direction.

[33] The flow speed is low near the two flanks. The flow speed is smaller in the region where N_{ps} is higher and T_{ps} is lower. The overall flow speed is lower when N_{sw} or $|B_{z,IMF}|$ is higher but is higher when V_{sw} is higher. The large-scale flow pattern remains almost unchanged under different interplanetary conditions. The speed of $\mathbf{V}_{dia}$ is larger near midnight and larger in the pre-midnight than in the post-midnight sector, and in these regions its magnitude is comparable to the total drift.

[34] Figure 5c shows the electric drift $\mathbf{V}_E$ computed from subtracting diamagnetic drift from the total drift, and Figure 5d shows contours of electric potential integrated over electric field $\mathbf{E} = -\mathbf{V}_E \times \mathbf{B}$ at the center of the current sheet. The electric drift shows that flow in the $Y < 0$ region is mainly directed earthward and dawnward, while the flow in the $Y > 0$ region is earthward and duskward. The contours of the electric potential at smaller X are less dense near midnight than near the flanks, indicating smaller electric field near midnight, a feature that is expected from the effect of shielding electric field near the inner edge of the plasma sheet.

4.2. Electric and Magnetic Drift Paths and Phase Space Density

[35] If the particles are transported by electric and magnetic drift, the phase space density of a given μ should be conserved along the drift paths assuming there are no particles added or lost along the drift paths. Since this is a statistical study, we do not expect to see a perfect match between the drift paths and constant phase space in small regions. Therefore we investigate if the important large-scale features seen in the distributions of phase space density can be explained by the drift transport.

[36] Figure 6 shows the contours of constant $\mu B + e\Phi$, which are equivalent to the electric and magnetic drift paths since the drift is $\mu\mathbf{B} \times \nabla B/eB^2 + \mathbf{B} \times \nabla\Phi/B^2$, and the phase space density normalized to N_{sw} (f_N) of ions and electrons of

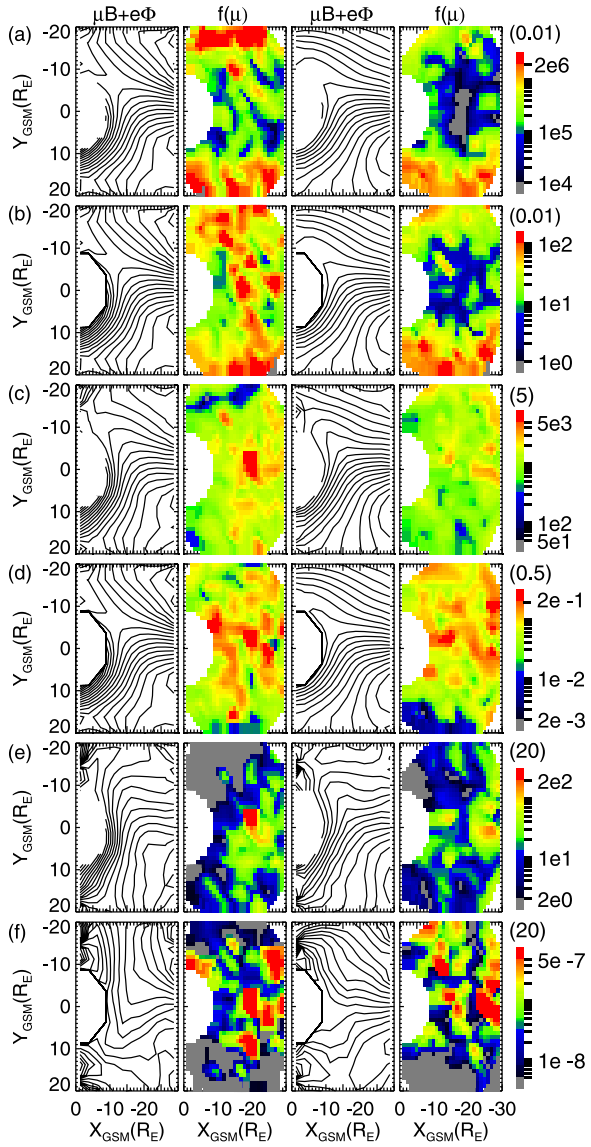

Figure 6. Comparisons between the drift paths ($\mu B + e\Phi$) and the distributions of phase space density normalized to the solar wind density (m^{-6} s^{-3} cm^3) for different μ (μ value in keV/10 nT, as indicated by the number above each color bar). The first and second columns are for the interplanetary condition (4) and the third and fourth columns are for the condition (8). Rows (a), (c), and (e) are for ions, and (b), (d), (f) are for electrons.

different energies under conditions (4) and (8). We chose conditions (4) and (8) because the low-energy f_N is significantly different under these two interplanetary conditions. It can be clearly seen, for very low energy ions and electrons (μ = 0.01 keV/10 nT), that the f_N peaks near the flanks and decreases with decreasing $|Y|$. The f_N near the dusk flanks are similar between these two conditions. However, the f_N near the dawn flank and near the midnight region is much higher in condition (4) than in condition (8), as we have pointed out in Section 3.3. For condition (8), the f_N near midnight is about two orders of magnitude lower than the peak f_N values near the flanks. These low energy particles are supposed to be dominated by electric drift as indicated in the transport paths. However, the high f_N near the flanks is much higher than the f_N in the tail, indicating they are not transported from the tail. However, if these particles are from the flanks, then the drift directions, which are pointed toward larger $|Y|$, will not allow the particles from the flanks to go toward smaller $|Y|$. However, a large f_N is seen to extend from the flanks to smaller $|Y|$ ($>\sim 10\ R_E$). These suggest other transport processes, such as diffusion, might play a role in transporting these particles inward from the flanks. This will be discusses in Section 5.1.

[37] That the higher phase space density for low energy particles with decreasing V_{sw} occurs only in the region from the dawn flank to around midnight but not near the dusk flank may suggest those cold particles are from the dawn flank, not from the distant tail. This is because, if the cold particles were mainly from the distant tail, it should also increase the phase space density near the dusk flank following the electric drift paths, which is not seen. Therefore the majority of low energy particles in the plasma sheet are from the flank source.

[38] The directions of electric drift are pointed toward larger $|Y|$, therefore low energy particles are pushed away midnight as they drift earthward. This explains the f_N for $\mu <$ 1 keV/10 nT shown in Figures 3 and 4 near midnight region is smaller in the near-Earth than that in the mid-tail.

[39] For near-thermal energy particles (μ = 5 keV/10 nT for ions and μ = 0.5 keV/10 nT for electrons) the f_N is relatively uniform throughout the plasma sheet compared to the low and high-energy particles. As expected from the drift paths shown in Figures 6c and 6d, particles from the tail can have access to the majority of the plasma sheet region. The f_N is slightly lower near the flanks. This is probably due to the plasma from the tail having slightly lower f near the flanks than near midnight.

[40] For high-energy particles (μ = 20 keV/10 nT), the drift paths indicate that there is a region in the near-Earth plasma sheet near dawn (dusk) that cannot be accessed by ions (electrons) from the tail due to ion's (electron's) duskward (dawnward) magnetic drift. Since there is no strong source for high-energy particles along the flanks, the f_N is significantly lower in the region where particles from the tail have no access. This strong dawn-dusk asymmetry is clearly seen in the f_N distributions.

[41] In general, the statistical study of the drift paths and distributions of phase space density versus energy indicates the electric and magnetic drifts are likely the dominant transport for thermal and high-energy ions and electrons from the tail sources. However, mechanisms other than electric and magnetic drift are needed to transport the low energy particles from the particle source at the flanks to the near-midnight region.

5. Discussion

5.1. Diffusion Transport

[42] Low energy particle motion is dominated by electric drift. With electric drift speed ~20 km/s (Figure 5c), the timescale for the plasma sheet particle drifting 1 R_E is on the order of above 1 min. Considering that the number of low energy particles entering from the flanks is much larger than the low energy particles from the tail, then a

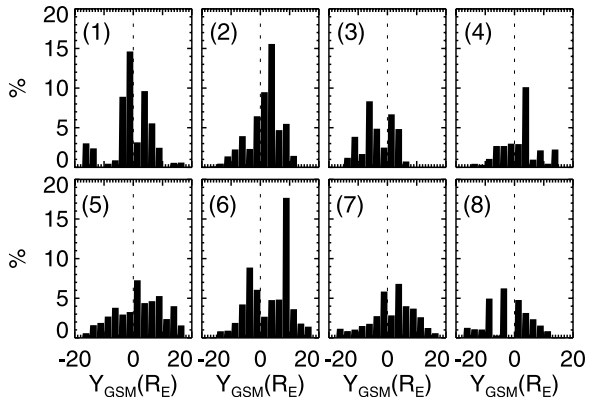

Figure 7. The Y profiles of the occurrence rate for earthward fast flow (>300 km/s) in the plasma sheet at X = 15 to 30 R_E for the 8 interplanetary conditions.

strong gradient is setup with the phase space density decreasing sharply away from the flanks. With this strong phase space density gradient, fluctuations in the electric drift direction can diffuse the low energy particles at the flanks toward midnight. This diffusion process has been proposed to populate cold particles in the plasma sheet [*Terasawa et al.*, 1997; *Wing et al.*, 2006]. Consistent with this proposal, fluctuations in the plasma flow direction with periods larger than 1 min during quiet time have been observed [*Angelopoulos et al.*, 1993]. These low frequency perturbations could be generated near the magnetopause, such as by Kelvin-Helmholtz instability [*Otto and Fairfield*, 2000], lower hybrid drift [*Winske and Omidi*, 1995], or kinetic Alfvén waves [*Johnson and Cheng*, 1997]. Cold particles may diffuse from the flanks at the same X distance, or may diffuse from the flanks further down the tail and then drift earthward.

[43] As discussed in Section 4.2, there are more cold particles near the dawn flank when V_{sw} is lower than when V_{sw} is higher, setting up a stronger gradient in phase space density in the Y direction. This stronger dawn flank source and gradient may allow more cold particles to diffuse to the near-midnight region, which provides an explanation for the higher phase space density of low energy particles in the mid-tail near-midnight region when V_{sw} is lower. Numerical simulations of diffusion are needed to test if diffusion can indeed transport cold particles from the flanks to midnight in a reasonable timescale.

5.2. Fast Bursty Bulk Flow

[44] Fast (>300 km/s) bursty bulk flow (BBF) in the perpendicular direction is often observed in the mid-tail plasma sheet. The plasma inside BBFs is observed to be hotter and more tenuous than that outside BBFs. Therefore BBFs can play an important role in transporting high-energy particles to the near-Earth plasma sheet [e.g., *Kaufmann et al.*, 2005]. However, the mechanisms for BBFs are not well understood. Figure 7 shows the occurrence rate of fast earthward BBFs in the mid-tail obtained by including the plasma sheet data with $|V_\perp| > 200$ km/s in our data set. It can be clearly seen that the fast BBF are more confined to the near-midnight region when V_{sw} is lower and the occurrence is slightly lower when N_{sw} or |IMF B_z| is higher. Therefore the occurrence of the fast BBFs appears to be lower when or where the plasma is colder and denser. This anti-correlation could be due to colder and denser plasma creating a less satisfactory condition for the occurrence of BBFs. It could also be explained by the average plasma being colder and denser in response to there being fewer BBFs to bring hot and tenuous plasma from the tail beyond $X = -30$ R_E.

5.3. Contribution to the Storm-Time Ring Current

[45] As the IMF turns from northward to strongly southward as typically observed during storms, the plasma sheet particles from the preceding northward IMF period penetrate earthward to the inner magnetosphere. Therefore the significant difference in N IMF N_{ps} and T_{ps} between different interplanetary conditions as shown in Figure 1 implies very different development for the storm time ring current. The ring current consists of ions and electrons in the 10–200 keV energy range. Considering a typical storm-time magnetic field of ~300 nT at $r = 4$ R_E, the ring current population consists of particles of μ in ~0.3 to 6 keV/10 nT range. Therefore the plasma sheet ions below the ion thermal energy (~5 keV) and the plasma sheet electrons above the electron thermal energy (~0.5 keV) are important particle sources for the ring current. As shown in Figure 3, among the 8 conditions, the ion phase space density within $\mu = 0.3$ to 6 keV/10 nT range is highest under condition (4) and is lowest under condition (5) and the difference between them is about an order of magnitude. Opposite to this, for electrons within the $\mu = 0.3$ to 6 keV/10 nT range, as shown in Figure 4, the phase space density under condition (5) is larger than that under condition (4), but the difference is not as large as that seen in ions. Therefore the plasma sheet under more strongly northward IMF with higher N_{sw} and lower V_{sw} can provide more ions but less electrons for the storm-time ring current, and, since ions contribute much more than the electrons to the ring current pressure and the increase in ions is larger than is the decrease in electrons, can result in a stronger storm. Our plasma sheet results can be used as boundary conditions in a ring current model to more quantitatively estimate the contributions of these different northward IMF plasma sheet to the storm-time ring current.

6. Summary

[46] We have investigated statistically how, during northward IMF periods, the changes in the solar wind density, solar wind speed, or the magnitude of the northward IMF B_z affect the equatorial distributions of the ion and electron plasma sheet measured by Geotail. We have investigated if our current understanding of the particle sources and transport can account for the observed plasma sheet distributions.

[47] For both ions and electrons, the overall N_{ps}/N_{sw} is clearly higher when $|B_{z,IMF}|$ is higher and N_{ps}/N_{sw} in the mid-tail is higher when V_{sw} is lower, suggesting more efficient solar wind entry from the flanks when the $|B_{z,IMF}|$ is higher or V_{sw} is lower. The density (temperature) is higher (lower) near the flanks and lower (higher) near midnight under all conditions. The N_{ps} becomes higher as the T_{ps} becomes lower, indicating the increase of particles is larger in the low energy than the high-energy range.

[48] We fitted the particle energy spectrum with a two-components kappa distribution to separate the plasma into a cold and a hot population, and to better estimate the cold population below the instrument's lower cutoff energy. For both ions and electrons, the contribution to the density from the cold population (<2 keV ions and <0.1 keV electrons) increases and become more dominant toward the flanks. In the near-Earth plasma sheet, the main contribution to the number density is from the hot population. These are consistent with the results from the DMSP observations [*Wing et al.*, 2005]. The different mixtures of the cold and hot populations in different regions are consistent with our understanding of the particle sources with colder particles coming from the flanks and hotter particles from the distant tail.

[49] The overall phase space density f at low energy increases with increasing $|B_{z,\mathrm{IMF}}|$. The f near the dawn flank and the f in the mid-tail near midnight region are significantly higher with decreasing V_{sw}, while the f near the dusk flank does not change as significantly. This suggests the solar wind entry through the dawn flank becomes more efficient when V_{sw} is lower. The f above thermal energy range in the pre-midnight sector is higher (lower) than that in the post-midnight sector for ions (electrons), and dawn-dusk asymmetries become stronger with increasing energy.

[50] We estimated electric and magnetic drift paths of ions and electrons versus different first adiabatic invariants from the observations. The comparisons with the distributions of constant f show that the electric and magnetic drifts are the major transport for particles of thermal and high energy. However, the electric and magnetic drift alone cannot explain the distributions of low energy particles, which peak along the flanks and decrease significantly toward midnight. That the particle source at the flanks sets up a strong gradient in the phase space density for low energy particles and observed long period perturbations in plasma drift flows suggests that the condition is suitable for diffusion to bring these cold particles from the flanks to midnight to account for the observed phase space density in the near-midnight region.

[51] The 0.3 to 6 keV ions and electrons in the plasma sheet are important sources for the ring current population and the difference between these sources under different interplanetary conditions during N IMF periods can be an order of magnitude, suggesting the resulting ring current can create significantly different storms or substorms.

[52] **Acknowledgments.** The work by C.-P. Wang and L. R. Lyons has been supported by NSF grant ATM- 0207298 and NASA grant NNX07AG42G. The work by J. M. Weygand has been supported by GEM grant ATM 02-1798 and NASA Research 1 AU grant NG-04GA93G. The work by R. W. McEntire has been supported by NASA Grant NNG04GC23G. We thank T. Mukai at ISAS and CDAWeb for the use of the Geotail LEP data. The Geotail magnetic field data are provided through the DARTS system by ISAS. We thank Jon Vandegriff of the Applied Physics Laboratory for providing the Geotail EPIC data. We also thank Dan Weimer for providing the Weimer variance analysis routine.

[53] Amitava Bhattacharjee thanks Andreas Keiling and Robert McPherron for their assistance in evaluating this paper.

References

Angelopoulos, V., et al. (1993), Characteristics of ion flow in the quiet state of the inner plasma sheet, *Geophys. Res. Lett.*, *20*, 1711–1714.

Borovsky, J. E., M. F. Thomsen, and R. C. Elphic (1998), The driving of the plasma sheet by the solar wind, *J. Geophys. Res.*, *103*(A8), 17,617–17,640.

Fujimoto, M., T. Terasawa, and T. Mukai (1998), The low-latitude boundary layer in the tail-franks, in *New perspectives on the Earth's magnetotail*, *Geophys. Monogr. Ser.*, vol. 105, edited by A. Nishida, D. N. Baker, and S. W. H. Cowley, pp. 33–44, AGU, Washington D. C.

Garner, T. W., R. A. Wolf, R. W. Spiro, M. F. Thomsen, and H. Korth (2003), Pressure balance inconsistency exhibited in a statistical model of magnetospheric plasma, *J. Geophys. Res.*, *108*(A8), 1331, doi:10.1029/2003JA009877.

Johnson, J. R., and C. Z. Cheng (1997), Kinetic Alfvén waves and plasma transport at the magnetopause, *Geophys. Res. Lett.*, *24*(11), 1423–1426.

Kaufmann, R. L., W. R. Paterson, and L. A. Frank (2004), Pressure, volume, density relationships in the plasma sheet, *J. Geophys. Res.*, *109*, A08204, doi:10.1029/2003JA010317.

Kaufmann, R. L., W. R. Paterson, and L. A. Frank (2005), Relationships between the ion flow speed, magnetic flux transport rate, and other plasma sheet parameters, *J. Geophys. Res.*, *110*, A09216, doi:10.1029/2005JA011068.

Kokubun, S., T. Yamamoto, M. H. Acuna, K. Hayashi, K. Shiokawa, and H. Kawano (1994), The Geotail magnetic field experiment, *J. Geomag. Geoelectr.*, *46*, 7–21.

Lavraud, B., M. F. Thomsen, J. E. Borovsky, M. H. Denton, and T. I. Pulkkinen (2006), Magnetosphere preconditioning under northward IMF: Evidence from the study of coronal mass ejection and corotating interaction region geoeffectiveness, *J. Geophys. Res.*, *111*, A09208, doi:10.1029/2005JA011566.

Lyons, L. R., and T. W. Speiser (1982), Evidence for current sheet acceleration in the geomagnetic tail, *J. Geophys. Res.*, *87*, 2276–2286.

Mukai, T., S. Machida, Y. Saito, M. Hirahara, T. Terasawa, N. Kaya, T. Obara, M. Ejiri, and A. Nishida (1994), The low-energy particle (LEP) experiment onboard the Geotail satellite, *J. Geomagn. Geoelectr.*, *46*, 669–692.

Nakamura, M., G. Paschmann, W. Baumjohann, and N. Sckopke (1991), Ions distributions and flows near the neutral sheet, *J. Geophys. Res.*, *96*, 5631–5649.

Øieroset, M., T. D. Phan, M. Fujimoto, L. Chan, R. P. Lin, and R. Skoug (2003), Spatial and temporal variations of the cold dense plasma sheet: evidence for a low-latitude boundary layer source?, in *Earth's Low-Latitude Boundary Layer*, edited by P. T. Newell and T. Onsager, pp. 253–264, AGU, Washington, D. C.

Otto, A., and D. H. Fairfield (2000), Kelvin-Helmholtz instability at the magnetotail boundary: MHD simulation and comparison with Geotail observations, *J. Geophys. Res.*, *105*(A9), 21,175–21,190.

Spence, H. E., and M. G. Kivelson (1993), Contributions of the low-latitude boundary layer to the finite width magnetotail convection model, *J. Geophys. Res.*, *98*, 15,487–15,496.

Terasawa, T., M. Fujimoto, T. Mukai, I. Shinohara, Y. Saito, T. Yamamoto, S. Machida, S. Kokubun, A. J. Lazarus, J. T. Steinberg, and R. P. Lepping (1997), Solar wind control of density and temperature in the near-Earth plasma sheet: WIND/Geotail collaboration, *Geophys. Res. Lett.*, *24*, 935–938.

Thomsen, M. F., J. E. Borovsky, R. M. Skoug, and C. W. Smith (2003), Delivery of cold, dense plasma sheet material into the near-Earth region, *J. Geophys. Res.*, *108*(A4), 1151, doi:10.1029/2002JA009544.

Tsyganenko, N. A., and T. Mukai (2003), Tail plasma sheet models derived from Geotail particle data, *J. Geophys. Res.*, *108*(A3), 1136, doi:10.1029/2002JA009707.

Wang, C.-P., L. R. Lyons, J. M. Weygand, T. Nagai, and R. W. McEntire (2006), Equatorial distributions of the plasma sheet ions, their electric and magnetic drifts, and magnetic fields under different interplanetary magnetic field Bz conditions, *J. Geophys. Res.*, *111*, A04215, doi:10.1029/2005JA011545.

Weimer, D. R., D. M. Ober, N. C. Maynard, M. R. Collier, D. J. McComas, N. F. Ness, C. W. Smith, and J. Watermann (2003), Predicting interplanetary magnetic field (IMF) propagation delay times using the minimum variance technique, *J. Geophys. Res.*, *108*(A1), 1026, doi:10.1029/2002JA009405.

Williams, D. J., R. W. McEntire, C. Schlemm II, A. T. T. Lui, G. Gloeckler, S. P. Christon, and F. Gliem (1994), GEOTAIL energetic particles and ion composition instrument, *J. Geomag. Geoelectr.*, *46*, 39–57.

Wing, S., and P. T. Newell (2002), 2D plasma sheet ion density and temperature profiles for northward and southward IMF, *Geophys. Res. Lett.*, *29*(9), 1307, doi:10.1029/2001GL013950.

Wing, S., J. R. Johnson, P. T. Newell, and C.-I. Meng (2005), Dawn-dusk asymmetries, ion spectra, and sources in the northward interplanetary magnetic field plasma sheet, *J. Geophys. Res.*, *110*, A08205, doi:10.1029/2005JA011086.

Wing, S., J. R. Johnson, and M. Fujimoto (2006), Timescale for the formation of the cold-dense plasma sheet: A case study, *Geophys. Res. Lett.*, *33*, L23106, doi:10.1029/2006GL027110.

Winske, D., and N. Omidi (1995), Diffusion at the magnetopause: Hybrid simulations, *J. Geophys. Res.*, *100*(A7), 11,923–11,934.

L. R. Lyons and C.-P. Wang, Department of Atmospheric and Oceanic Sciences, University of California, Los Angeles, CA, USA. (cat@atmos.ucla.edu)

R. W. McEntire, Applied Physics Laboratory, Johns Hopkins University, Laurel, MD, USA.

T. Nagai, Department of Earth and Planetary Sciences, Tokyo Institute of Technology, Tokyo, Japan.

J. M. Weygand, Institute of Geophysics and Planetary Physics, University of California, Los Angeles, CA, USA.